Catalysis Science & Technology

ROYAL SOCIETY OF CHEMISTRY

PAPER

Published on 17 September 2026
Licence and permissions

Check for updates

Cite this: *Catal. Sci. Technol.*, 2026, **16**, 7342

Interfacial coupling in a CdSe/Ni-MOLs heterojunction for visible-light-driven photocatalytic hydrogen evolution

Hongyan Zhao, Yu Li, Yifan Liao, Jiayi Meng, Quanmei Zhou, Yuchen Wei, Yuying Hu, Mohan Zhang, Bite Deng, Yamei Huang and Wei-Lin Dai *

Photocatalytic hydrogen evolution represents a sustainable and eco-friendly strategy for hydrogen production, yet its efficiency is fundamentally limited by the high-rate recombination of photo-induced electron–hole pairs. Constructing heterojunctions is a pivotal strategy to overcome this limitation. In this study, we report a novel binary heterojunction composed of CdSe nanorods and Ni-based metal–organic layers (Ni-MOLs) nanosheets, fabricated *via* an *in situ* solvothermal approach. A series of CdSe/Ni-MOLs composites (denoted as CNM-*x*) were prepared. The optimized CNM-0.5 exhibited a high hydrogen evolution rate of 10.77 mmol g^{-1} h^{-1}, which was 38 and 160 times higher than that of pristine CdSe and Ni-MOLs, respectively. Meanwhile, the optimized photocatalyst demonstrated excellent stability over five consecutive cycles, together with an apparent quantum efficiency (AQE) of 7.3% (350 nm). *In situ* and ultrafast spectroscopic analyses coupled with density functional theory (DFT) calculations systematically elucidate the synergistic mechanism within the type-II heterojunction. The intimate interfacial coupling between CdSe and Ni-MOLs induces favorable charge redistribution, establishes a robust built-in electric field, and drives directional electron transfer from CdSe to Ni-MOLs active sites with a prolonged carrier lifetime, effectively suppressing charge recombination and lowering the Gibbs free energy for hydrogen adsorption. This study underscores the potential of dimensionally matched heterostructures in suppressing charge recombination and provides strategic insights into the rational design of MOLs-based systems for efficient solar-driven hydrogen production.

Received 12th May 2026,
Accepted 16th September 2026

DOI: 10.1039/d6cy00639f

rsc.li/catalysis

Introduction

The escalating global demand for energy, coupled with pressing environmental imperatives, has catalyzed the pursuit of sustainable and clean energy technologies.[1–8] Hydrogen, owing to its renewable, clean, and efficient characteristics, is increasingly heralded as a pivotal green energy vector for a sustainable future.[9–13] From this perspective, solar-to-hydrogen conversion *via* photocatalysis represents a strategic avenue with immense development potential.[14,15] Insufficient structural diversity, coupled with the ultrafast recombination of photo-excited charge carriers, often curtails the performance of conventional inorganic semiconductors like TiO_2 and CdS.[16–18] To overcome these electronic bottlenecks, constructing heterojunction architectures has been recognized as a frontline strategy to modulate interfacial charge separation, accelerate reaction kinetics, and boost hydrogen evolution performance.[19,20]

In recent years, a diverse array of emerging photocatalytic platforms, including metal–organic frameworks (MOFs),[21–26] g-C_3N_4,[27–33] metal sulfides,[34–39] and metal selenides,[40–44] have been extensively explored for solar energy conversion. Among these, MOFs represent a class of porous crystalline frameworks constructed through the coordination of metal nodes or clusters with organic linkers, featuring expansive specific surface areas, highly tunable structures, and an abundance of accessible active sites.[45–51] As two-dimensional (2D) congeners of their 3D counterparts, metal–organic layers (MOLs) inherit the structural periodicity and chemical versatility of MOFs while offering distinct kinetic advantages. Their unique monolayer configuration not only exposes more active sites but also significantly abbreviates the diffusion pathways for both reactants and photogenerated carriers.[52,53] Although many MOLs have been explored for photocatalytic energy conversion,[54–57] most pristine MOLs-based photocatalysts still exhibit suboptimal visible-light harvesting and rapid charge recombination, particularly in the absence of noble-metal cocatalysts or photosensitizers.[58,59] Consequently, integrating MOLs into heterojunction architectures emerges as a compelling strategy to

State Key Laboratory of Porous Materials for Separation and Conversion, Shanghai Key Laboratory of Molecular Catalysis and Innovative Materials, Department of Chemistry, Fudan University, Shanghai 200438, P. R. China.
E-mail: wldai@fudan.edu.cn

This journal is © The Royal Society of Chemistry 2026

synergistically facilitate charge separation and bolster hydrogen evolution performance, rendering the development of highly efficient MOLs-based heterostructures a pursuit of paramount importance.

CdSe has emerged as a compelling candidate for visible-light-driven photocatalysis, owing to its suitable bandgap, robust light-harvesting capacity, and advantageous charge-carrier mobility.[60–62] The catalytic efficacy of pristine CdSe is fundamentally hampered by a dual constraint: the facile recombination of photo-excited charges and a paucity of accessible catalytic centers on its surface. To circumvent these limitations, the fabrication of CdSe-based heterostructures has gained prominence as a potent approach to promote spatial charge separation and modulate interfacial electronic communication.[63,64]

Inspired by these imperatives, a 1D/2D CdSe/Ni-MOLs heterojunction is herein reported, synthesized through an *in situ* solvothermal route wherein 2D Ni-MOLs nanosheets serve as structural scaffolds for the growth of 1D CdSe nanorods. The optimized composite, denoted as CNM-0.5, yielded a peak hydrogen evolution rate of 10.77 mmol g^{-1} h^{-1}, representing 38-fold and 160-fold improvements compared with pristine CdSe and Ni-MOLs, respectively. Detailed investigations reveal that this integrated 1D/2D architecture not only broadens the optical response but also significantly accelerates the separation and transfer of photogenerated carriers. This work underscores the efficacy of dimensional engineering in constructing high-performance heterojunctions for photocatalytic proton reduction to H_2.

Experimental

Synthesis of CdSe samples

CdSe nanorods were synthesized *via* a solvothermal method. Briefly, deionized water (6 mL), diethylenetriamine (DETA, 18 mL), and hydrazine hydrate ($N_2H_4{\cdot}H_2O$, 12 mL) were added into a 100 mL polytetrafluoroethylene (PTFE) reactor and stirred for 10 min to form a homogeneous solution. Subsequently, $CdCl_2{\cdot}2.5H_2O$ (228 mg, 1.0 mmol) and Se powder (90 mg, 1.0 mmol) were added to the mixture, followed by stirring at 25 °C for 1 h. The obtained solution was sealed in a stainless-steel autoclave and thermally treated at 100 °C for 12 h. Upon reaching ambient temperature spontaneously, the precipitate was collected by centrifugation and subjected to three washing-centrifugation cycles with deionized water and ethanol. The resulting product was lyophilized for 18 h, finally yielding the brick-red CdSe nanorods.

Synthesis of Ni-MOLs samples

Ni-MOLs were fabricated following an established hydrothermal protocol.[65] Briefly, H_2BDC (0.166 g) and $Ni(NO_3)_2{\cdot}6H_2O$ (0.436 g) were dispersed in 15 mL of DMF under continuous stirring, followed by the dropwise addition of 2 mL of NaOH solution (0.04 mol L^{-1}). The resulting mixture was encapsulated in a 100 mL Teflon-lined stainless-steel reactor and thermally processed at 120 °C for 10 h. Once the system equilibrated to ambient temperature, the green precipitates were recovered by centrifugation and purified through three rinsing cycles with DMF and ethanol. Finally, the product was dried *in vacuo* at 50 °C to yield the Ni-MOLs samples.

Synthesis of CNM-*x* samples

The CNM-*x* composites (x = 0.1, 0.5, 1.5, and 3, representing the mass ratio of Ni-MOLs to CdSe) were synthesized *via* an *in situ* solvothermal route. In a typical synthesis of CNM-0.5, 110 mg of pre-synthesized Ni-MOLs were dispersed into the H_2O/DETA/$N_2H_4{\cdot}H_2O$ mixture as described in the Synthesis of CdSe samples section. Subsequently, $CdCl_2{\cdot}2.5H_2O$ and Se powder were added, and the solvothermal reaction and subsequent purification were conducted following the identical procedure for pristine CdSe. Other samples were prepared by adjusting the mass of Ni-MOLs accordingly. For comparison, a control CNM-0.5 sample was synthesized *via* an electrostatic self-assembly method by ultrasonically stirring a mixture of Ni-MOLs (50 mL water dispersion) and CdSe nanorods for 1 h.

Characterization and theoretical method

Material characterization, photocatalytic hydrogen evolution strategy, photoelectrochemical tests, and the detailed theoretical calculation method can be found in SI.

Results and discussion

Morphology and structure characterization

As depicted in Scheme 1, the CNM-*x* heterojunctions were engineered *via* a step-wise approach, where the first stage involved the hydrothermal synthesis of 2D Ni-MOLs nanosheets at 120 °C. These pre-synthesized nanosheets were subsequently introduced into a solvothermal system to serve as templates for the *in situ* nucleation and growth of 1D CdSe nanorods. Specifically, by dispersing stoichiometric amounts of Ni-MOLs, $CdCl_2{\cdot}2.5H_2O$, and Se powder in a mixed solvent of deionized water, DETA, and $N_2H_4{\cdot}H_2O$, the CNM-*x* composites were obtained after hydrothermal treatment at 100 °C for 12 h. This *in situ* growth strategy ensures intimate interfacial contact between the 1D nanorods and 2D nanosheets, resulting in the characteristic brick-red powders.

The morphologies and microstructures of pristine CdSe, Ni-MOLs, and the CNM-0.5 were systematically analyzed by

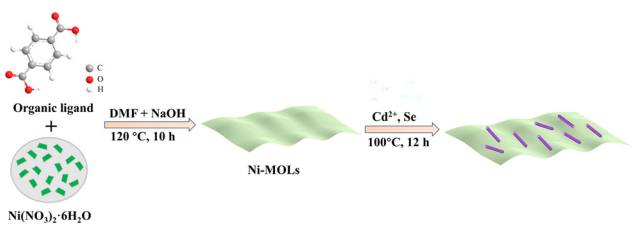

Scheme 1 Illustration of the fabrication protocol for CNM-*x*.

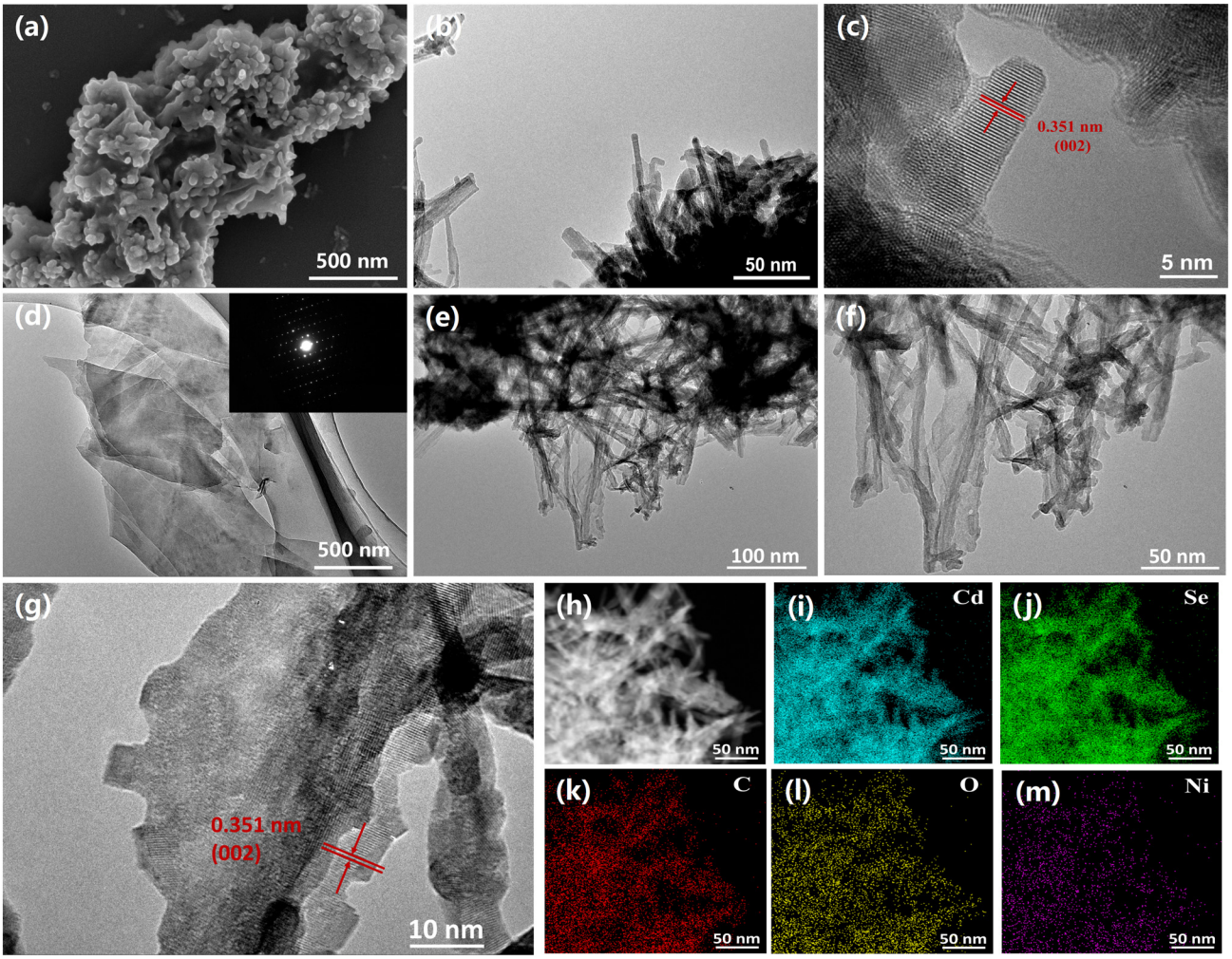

Fig. 1 (a) SEM, (b) TEM, and (c) HRTEM images of CdSe. (d) TEM image of Ni-MOLs (inset: SAED pattern). (e and f) TEM and (g) HRTEM images of CNM-0.5. (h) HAADF-STEM image and (i–m) corresponding EDS elemental maps of Cd, Se, C, O, and Ni for CNM-0.5.

SEM and TEM. As shown in Fig. 1a, S1a and S1b, CdSe exhibits a typical 1D nanorod morphology with a relatively smooth surface. High-resolution TEM (HRTEM) imaging reveals clear lattice fringes with an interplanar spacing of 0.351 nm (Fig. 1b and c), which is indexed to the (002) crystal plane of CdSe.[68] For pristine Ni-MOLs, a 2D layered morphology with a flat surface is observed in Fig. S2a–c, while the corresponding selected area electron diffraction (SAED) pattern confirms its single-crystalline nature (inset of Fig. 1d).[69,70] Regarding the CNM-0.5 heterojunction (Fig. 1e–g and S3), a 3D hierarchical framework is evident, where a high density of CdSe nanorods is intimately anchored onto the Ni-MOLs nanosheets. HRTEM analysis of the heterostructure (Fig. 1g) further confirms the presence of CdSe through the (002) lattice fringes,[66,68] and more importantly, reveals the close contact between the two components, suggesting the formation of a robust heterointerface. Additionally, EDS elemental mapping (Fig. 1h–m and S3e–j) demonstrates that Cd, Se, C, O, and Ni are uniformly distributed across the composite, further verifying the successful integration and high dispersion of the individual phases.

The CNM-0.5 synthesized *via* a physical mixing method driven by electrostatic self-assembly was also characterized by TEM. As depicted in Fig. S4, several dispersed and irregularly shaped CdSe nanorods can be observed adhering to the layered structure of Ni-MOLs.

XRD analysis was conducted to elucidate the crystalline nature of CNM-*x* (Fig. 2a). Pristine CdSe shows prominent

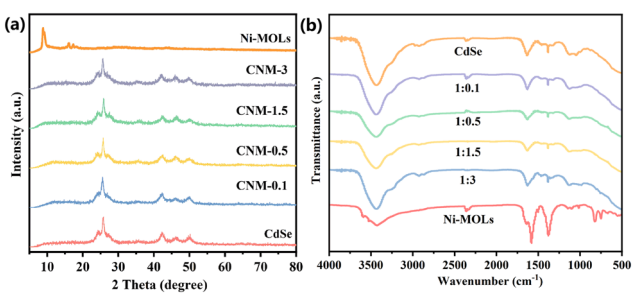

Fig. 2 (a) XRD patterns of CdSe, Ni-MOLs, and the CNM-*x* series (*x* = 0.1, 0.5, 1.5, and 3). (b) FT-IR spectra of CdSe, Ni-MOLs, and CNM-*x* composites.

This journal is © The Royal Society of Chemistry 2026

peaks corresponding to the (100), (002), (101), (102), (110), (103), and (112) planes of its hexagonal (wurtzite) structure.[66] Meanwhile, Ni-MOLs exhibit characteristic peaks at 8.5° and 16.9°, indexing to the (100) and (010) facets.[65] For CNM-*x*, the patterns remain dominated by CdSe without detectable shifts, which is attributed to the partial dissolution of the ordered structure of most Ni-MOLs during the synthesis process and their loss during washing, resulting in only a small amount of Ni-MOLs forming the heterostructure with CdSe. Furthermore, because Ni-MOLs are highly dispersed in the form of ultrathin layers, its diffraction peaks are barely discernible in the XRD patterns. Additionally, the FT-IR spectra (Fig. 2b) display a broad envelope centered at 3467 cm^{-1}, which originates from the O–H stretching vibrations. In addition, the vibrational features spanning 1413–1668 cm^{-1} can be unambiguously ascribed to the characteristic skeletal modes of aromatic rings alongside carbonyl functionalities.[57] The FT-IR profiles of the CNM-*x* heterojunctions resemble those of CdSe, with a gradual decrease in the intensity of CdSe-related features upon increasing the Ni-MOLs content. These results collectively confirm the successful construction of the CNM-*x* heterojunctions and suggest the existence of robust interfacial interactions between the two components.

To accurately evaluate the Ni loading in the CNM-*x* composites, inductively coupled plasma-atomic emission spectroscopy (ICP-AES) was performed. As summarized in Table S1, the Ni weight percentages for CNM-0.1, CNM-0.5, CNM-1.5, and CNM-3 were measured to be 0.03%, 0.44%, 0.32%, and 0.57%, respectively. These low loading levels are highly consistent with the absence of distinct Ni-related diffraction peaks in the XRD patterns and the local elemental distributions obtained from EDS. Notably, the measured Ni content does not follow a well-defined trend with the initial Ni-MOLs feeding ratios. Under higher precursor feeding ratios, the elevated ion concentration increases the ionic strength of the synthetic solution, which potentially perturbs the heterogeneous nucleation and growth kinetics. Concurrently, the increased ionic strength promotes the self-aggregation of ultrathin 2D Ni-MOLs nanosheets in the liquid phase, thereby weakening their heterogeneous assembly with CdSe. Because the interfacial binding between Ni-MOLs and CdSe is predominantly governed by weak coordination and electrostatic attractions, these loosely attached or aggregated Ni species readily detach from the CdSe substrate during subsequent centrifugation and washing, ultimately leading to a lower retained Ni loading in CNM-1.5 than in CNM-0.5. Nevertheless, these results, in conjunction with the catalytic performance, confirm that the moderate Ni content in CNM-0.5 achieves the optimal interfacial coupling efficiency, thereby constructing ideal channels for photogenerated charge transfer.

The thermogravimetric curves of CdSe, Ni-MOLs, and CdSe/Ni-MOLs further confirm the presence of Ni-MOLs in the composite, as shown in Fig. 3. Under a nitrogen atmosphere, CdSe exhibits a significant weight loss starting

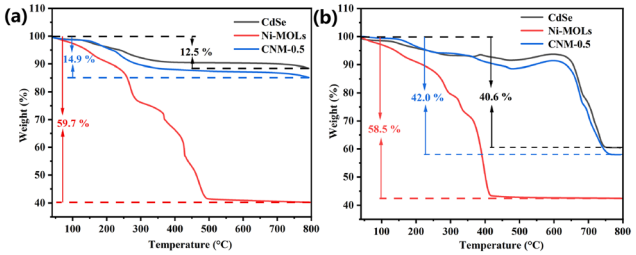

Fig. 3 TG curves of CdSe, Ni-MOLs and CNM-0.5 that calcined under (a) nitrogen and (b) air atmosphere.

at approximately 200 °C and stabilizes at about 87.5% at 500 °C, which is likely attributed to the decomposition or volatilization of adsorbed water or templating agents. Ni-MOLs show a slight weight loss at around 100 °C due to the evaporation of adsorbed water or organic solvents. A sharp increase in weight loss occurs at approximately 300 °C, eventually stabilizing at about 40% at around 500 °C, corresponding to the decomposition of organic functional groups within the Ni-MOLs. The CNM-0.5 composite displays two major weight loss stages at approximately 200 °C and 400 °C, with a final residual weight of about 85%, confirming its robust thermal stability at high temperatures. Under an air atmosphere, the weight loss of CdSe begins at approximately 200 °C and stabilizes at about 60% at 700 °C. Ni-MOLs exhibit minor weight loss at 100 °C followed by a substantial loss at approximately 300 °C, reaching a plateau of around 41.5% at 750 °C. The CNM-0.5 composite also shows two primary weight loss stages at approximately 200 °C and 400 °C, with a final weight of 58%. This indicates that the thermal stability of the composite in air is slightly lower than that in a nitrogen environment. Notably, the TGA curves of CNM-0.5 do not overlap with those of the individual components in either atmosphere; instead, they are positioned between the curves of CdSe and Ni-MOLs. This further demonstrates that the two components are not merely physically mixed but have successfully constructed a structurally stable binary heterojunction through interfacial coupling.

To gain deeper insights into the surface elemental distribution and electronic states of the CNM-0.5 heterostructure, X-ray photoelectron spectroscopy (XPS) was performed. The survey spectrum (Fig. S5) confirms the coexistence of Cd, Se, C and O elements within the heterostructure. Despite the low loading of Ni-MOLs, high-resolution core-level spectra clearly distinguish the characteristic peaks of Ni. As shown in Fig. 4a, the Cd $3d_{5/2}$ and Cd $3d_{3/2}$ peaks of CNM-0.5 are located at 404.4 eV and 411.3 eV, representing a positive shift of 0.2 eV compared to pristine CdSe (404.2 eV and 411.1 eV), which indicates that the variation in electron density modifies the local chemical environment of Cd. Similarly, Fig. 4b displays that the characteristic Se $3d_{5/2}$ and Se $3d_{3/2}$ peaks of CNM-0.5 shift positively to 53.2 eV and 54.0 eV (relative to 52.9 eV and 53.7 eV for pristine CdSe), further corroborating the electron

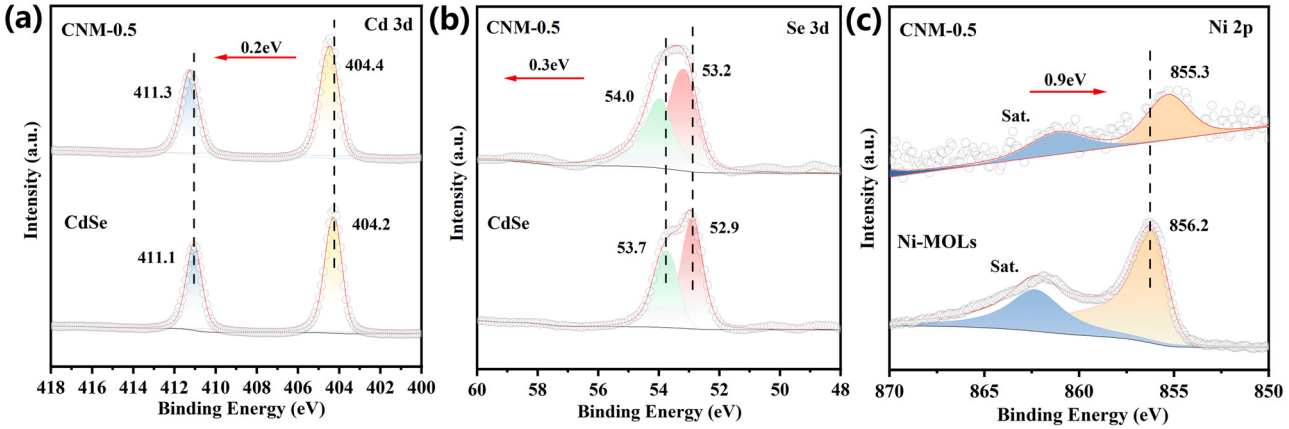

Fig. 4 High resolution XPS spectra of (a) Cd 3d, (b) Se 3d, (c) Ni 2p.

migration from CdSe to Ni-MOLs. In Fig. 4c, the Ni $2p_{3/2}$ binding energy of CNM-0.5 exhibits a substantial negative shift to 855.3 eV compared to pristine Ni-MOLs (856.2 eV). The concurrent positive shifts in Cd 3d and Se 3d along with the negative shift in Ni 2p provide compelling spectroscopic evidence for intimate interfacial electronic coupling and spontaneous ground-state electron transfer from CdSe to Ni-MOLs within the heterostructure.[71]

Photocatalytic performance of CNM-*x*

To systematically evaluate the performance of the photocatalyst, its visible-light-driven hydrogen evolution activity is tested, and the results are shown in Fig. 5a. Compared with pristine CdSe, all CNM-*x* composites exhibit significantly enhanced photocatalytic hydrogen evolution activity. Among them, CNM-0.5 demonstrates the optimal performance with a hydrogen evolution rate of 10.77 mmol g^{-1} h^{-1}, which is approximately 38 and 160 times higher than that of pristine CdSe (0.28 mmol g^{-1} h^{-1}) and Ni-MOLs (0.07 mmol g^{-1} h^{-1}), respectively. The superior performance is primarily attributed to the formation of an intimate heterojunction, which facilitates the efficient migration of photogenerated electrons and suppresses carrier recombination. However, a slight decline in activity was observed at higher Ni-MOLs loadings (CNM-1.5 and CNM-3), likely due to the competitive light absorption (shading effect) and/or the partial coverage of active sites. Furthermore, the influence of synthetic strategies was comparatively investigated (Fig. 5b). The sample prepared *via* the *in situ* growth of CdSe on Ni-MOLs (CNM-0.5) yielded the highest activity. In contrast, the samples synthesized by the inverse growth (Ni-MOLs on CdSe) and the electrostatic self-assembly method exhibited significantly lower rates of 0.21 and 0.13 mmol g^{-1} h^{-1}, respectively. These results underscore that the *in situ* solvothermal growth of CdSe onto Ni-MOLs scaffolds is the optimal route for constructing high-performance heterojunctions.

The photostability and durability of CNM-0.5 were assessed through five consecutive recycling runs (Fig. 5c), during which the composite maintained a stable and efficient PHE rate. Furthermore, the structural, chemical, and compositional stability of the post-reaction catalyst was systematically investigated using SEM, TEM, XRD, XPS, and ICP-AES analyses (Fig. S6–S9). SEM and TEM images reveal that the original morphology is well preserved, with clearly visible lattice fringes. The XRD pattern displays no discernible shifts in either peak positions or intensities of the characteristic diffraction peaks, while XPS spectra confirm that the binding energies and valence states of the constituent elements remain essentially unchanged. Additionally, ICP-AES analysis of the post-reaction solution revealed that the Ni concentration remained below 1 ppm, confirming negligible metal leaching throughout the photocatalytic process. These combined results demonstrate that the micromorphology, crystal structure, and surface chemical states of the catalyst undergo no significant degradation after multiple catalytic cycles, highlighting its exceptional structural and chemical stability under practical reaction conditions.

Additionally, the apparent quantum efficiency (AQE) was measured at multiple wavelengths (320, 350, 400, 420, 450, 500, 550 and 600 nm), as shown in Fig. 5d. Under monochromatic light at 350 nm, the AQE reached 7.3%. The trend of AQE values is consistent with the UV-vis diffuse reflectance spectrum of the CNM-0.5 heterojunction, confirming that the photocatalytic process is light-driven. Compared with other previously reported CdSe-based photocatalysts (Table S2), the CNM-0.5 composite stands out with its excellent hydrogen evolution activity.

The light-harvesting properties of the CNM-*x* composites are analyzed by UV-vis diffuse reflectance spectroscopy (UV-vis DRS). As shown in Fig. S10, pristine CdSe exhibits an absorption edge at approximately 700 nm, reflecting a broad visible-light response range. In contrast, the absorption edge of pristine Ni-MOLs is located near 500 nm, indicating limited visible-light utilization. Upon integration of the two components, the CNM-0.5 composite displays a markedly enhanced absorption intensity across the visible-light region compared to individual Ni-MOLs. The absorption spectrum of the heterojunction effectively encompasses the characteristic

 This journal is © The Royal Society of Chemistry 2026

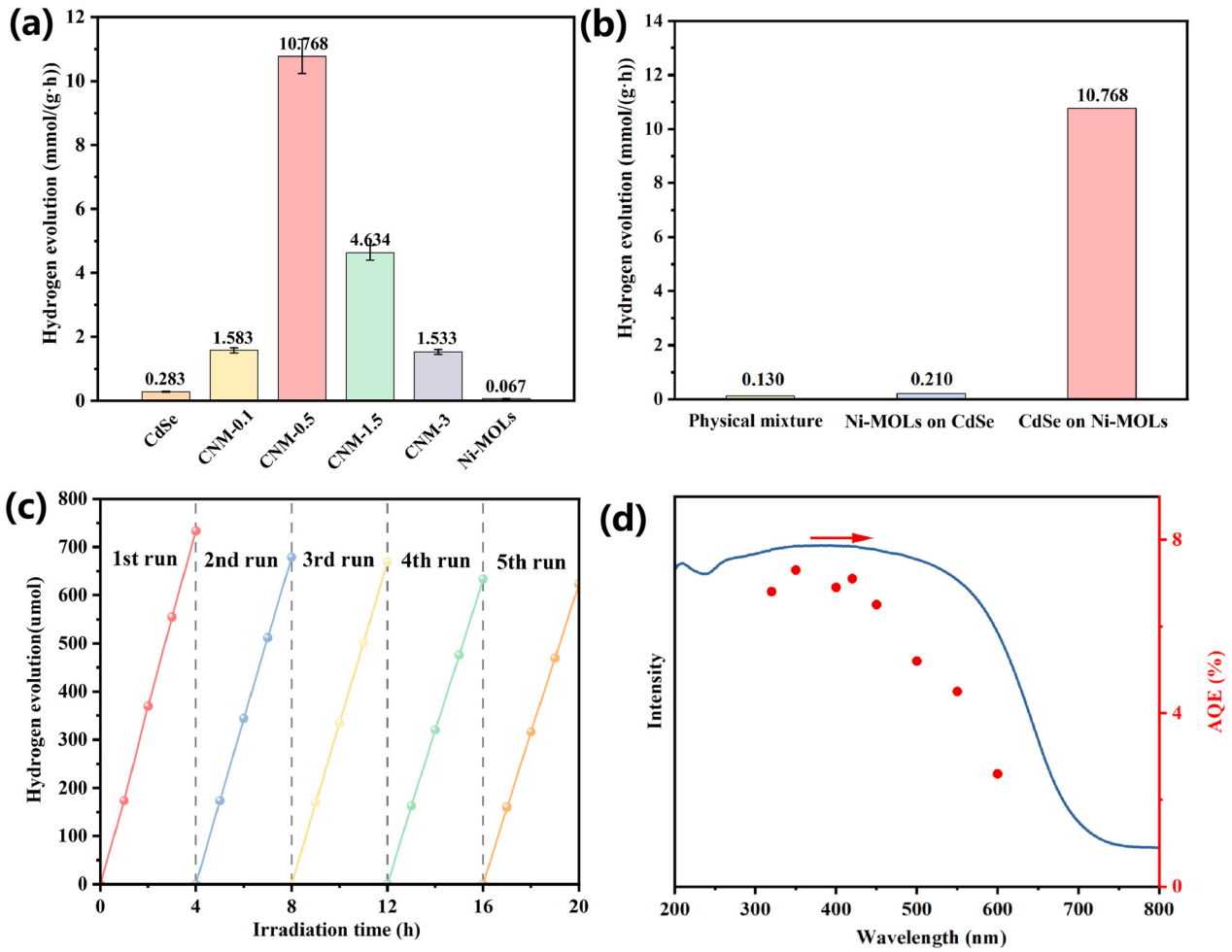

Fig. 5 (a) Comparison of H_2 evolution rates for CdSe, Ni-MOLs and CNM-*x* (*x* = 0.1, 0.5, 1.5, 3). The error bars represent the standard deviation from four independent measurements. (b) H_2 evolution rate of CNM-0.5 composites synthesized by different methods. (c) Recycling photocatalytic H_2 production test of CNM-0.5. (d) AQE of CNM-0.5.

ranges of both CdSe and Ni-MOLs, resulting in a broadened photoresponse. This optimized optical property is highly conducive to the generation of photogenerated carriers, thereby facilitating the overall photocatalytic efficiency.

Charge transfer efficiency

To elucidate the underlying mechanism responsible for the enhanced photocatalytic performance of the CNM-*x* heterojunctions, electrochemical impedance spectroscopy (EIS), transient photocurrent response, and photoluminescence measurements are systematically conducted. As shown in Fig. 6a, the CNM-0.5 composite exhibits the smallest impedance semicircle radius among the tested samples, indicating the lowest charge-transfer resistance and superior carrier transport efficiency.[63] Concurrently, CNM-0.5 delivers the highest photocurrent density (Fig. 6b), confirming efficient spatial separation and rapid interfacial migration of photogenerated electron–hole pairs across the heterojunction.[64] To further probe the carrier dynamics, steady-state photoluminescence (PL) and time-resolved photoluminescence (TRPL) spectra are collected. As displayed in Fig. S11, pristine CdSe exhibits a strong emission peak centered around 608 nm, whereas the PL intensity of the CNM-0.5 composite drops significantly, suggesting that the radiative recombination of photogenerated electron–hole pairs is effectively suppressed. Moreover, the TRPL decay spectra (Fig. 6c) reveal that the average carrier lifetime is shortened from 10.410 ns for pristine CdSe to 2.668 ns for CNM-0.5. This pronounced lifetime reduction directly demonstrates the establishment of an ultrafast non-radiative electron transfer pathway from CdSe to Ni-MOLs, which effectively suppresses radiative charge recombination.[67] Consequently, the CNM-0.5 composite catalyst accelerates interfacial charge transfer kinetics and promotes spatial charge separation, highlighting its enormous potential for photocatalytic applications.

Theoretical calculation and photocatalytic mechanism

The direction of charge transfer in the CNM-0.5 heterojunction was verified by *in situ* irradiated XPS analysis.

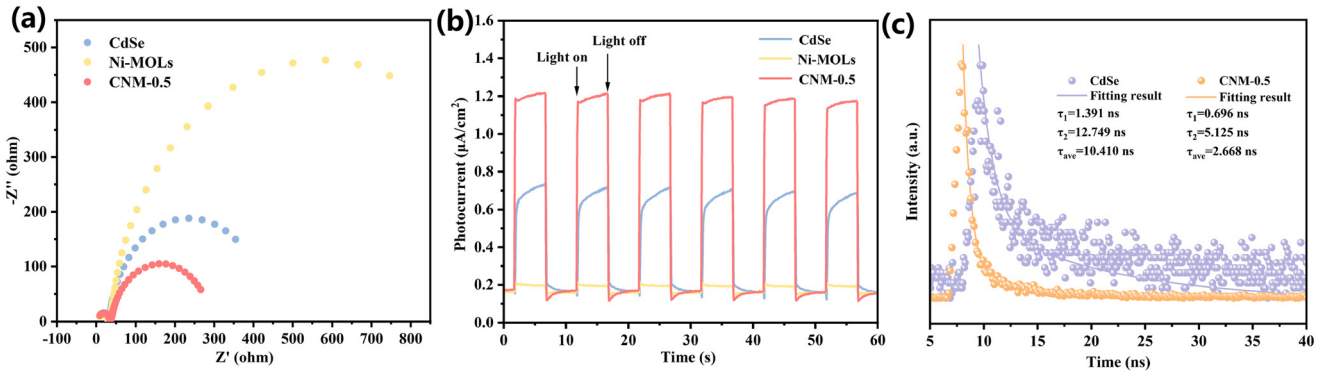

Fig. 6 (a) EIS Nyquist plots, (b) photocurrent responses, (c) time-resolved PL spectra of samples.

As shown in Fig. 7a, upon light irradiation, the characteristic Cd $3d_{3/2}$ and Cd $3d_{5/2}$ peaks of CNM-0.5 both undergo a positive shift of 0.2 eV. Similarly, the Se $3d_{3/2}$ and Se $3d_{5/2}$ doublets positively shift by 0.2 eV to higher binding energies under illumination (Fig. 7b). These concomitant shifts toward higher binding energy clearly indicate decreased

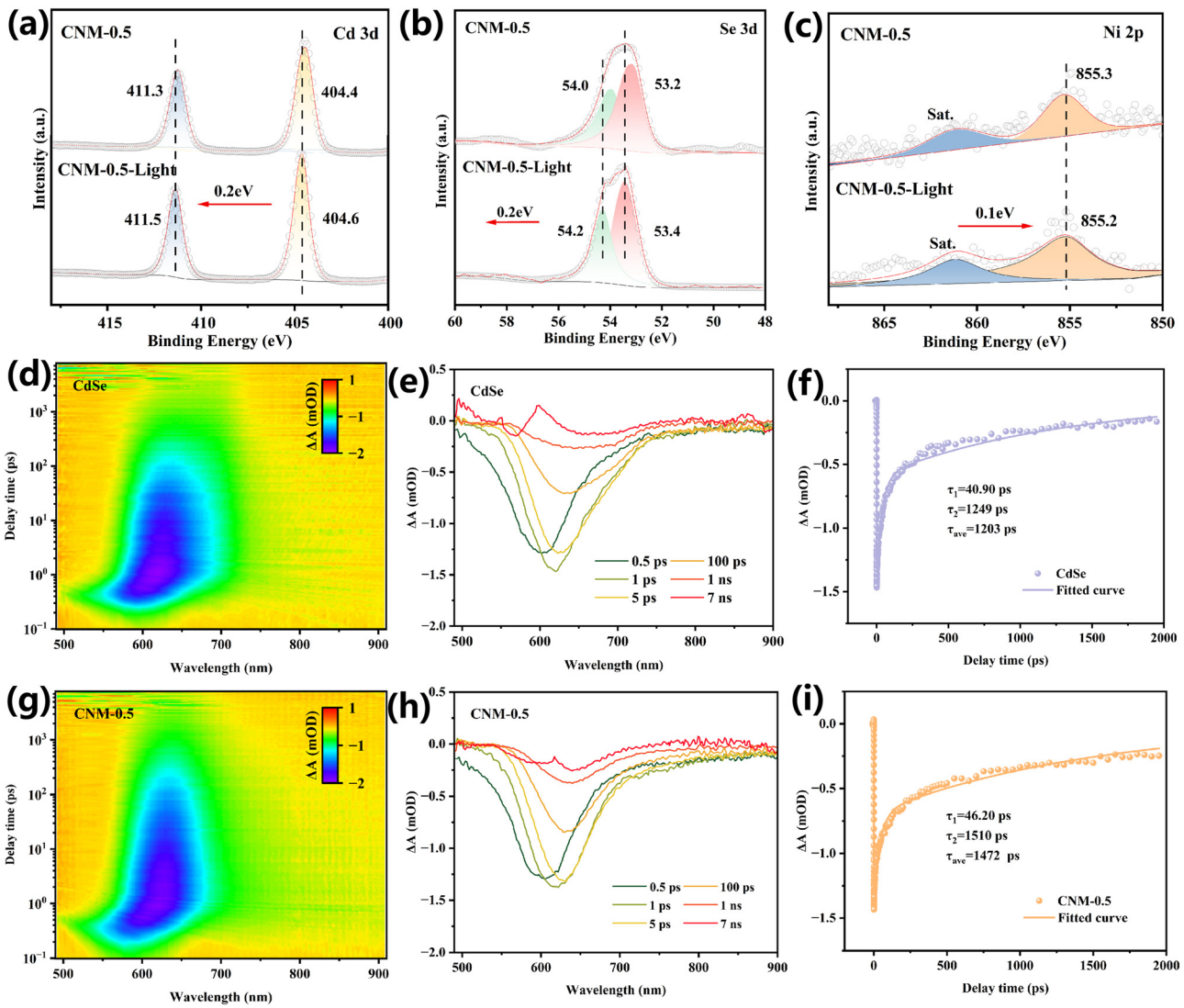

Fig. 7 High-resolution *in situ* XPS spectra of (a) Cd 3d, (b) Se 3d, (c) Ni 2p of CNM-0.5. (d and g) Contour plots of transient absorption spectra for CdSe and CNM-0.5. (e and h) TAS recorded at indicated delay time, (f and i) normalized decay kinetic curves for CdSe and CNM-0.5.

 This journal is © The Royal Society of Chemistry 2026

electron density on the CdSe component resulting from photoinduced electron depletion. In contrast, the Ni $2p_{3/2}$ peak shifts toward a lower binding energy by 0.1 eV (from 855.3 to 855.2 eV) under the same irradiation conditions (Fig. 7c), confirming an increase in electron density around the Ni sites. These results demonstrate that photogenerated electrons transfer from CdSe to Ni-MOLs under light irradiation. In this system, Ni-MOLs act as efficient electron sinks, facilitating spatial charge separation and suppressing carrier recombination, which ultimately leads to a substantial improvement in photocatalytic hydrogen evolution performance.

Femtosecond transient absorption spectroscopy (fs-TAS) is employed to track the generation, separation, and recombination dynamics of photogenerated charge carriers in pristine CdSe and the CNM-0.5 heterojunction. As shown in Fig. 7, both pristine CdSe (Fig. 7d–f) and the CNM-0.5 composite (Fig. 7g–i) display typical transient absorption features across the visible region, characterized by a prominent negative signal centered at 620 nm. This negative band is assigned to ground-state bleaching (GSB), which originates from the pump-induced transition of electrons from the valence band to the conduction band of CdSe, resulting in state filling and reduced absorption at the probe wavelength. Because the optical response is dominated by this intrinsic CdSe GSB feature, the kinetic decay profiles at 620 nm are selected to trace the excited-state carrier evolution.

The spectral evolution at distinct delay times demonstrates that both samples rapidly reach maximum bleaching intensity on a sub-picosecond timescale, followed by a gradual decay toward the baseline. Notably, CNM-0.5 exhibits a noticeably slower GSB recovery rate at extended delay times, confirming that the introduction of Ni-MOLs modulates the excited-state relaxation dynamics of CdSe. Multi-exponential fitting reveals that the average carrier lifetime increases from 1203 ps for pristine CdSe to 1472 ps for CNM-0.5.

These fs-TAS findings provide compelling, complementary evidence alongside the TRPL results. While the TRPL lifetime dramatically decreases from 10.410 ns to 2.668 ns due to rapid electron injection from the conduction band of CdSe into CNM, the prolonged GSB lifetime confirms that the remaining valence band holes cannot rapidly recombine with electrons due to effective spatial charge separation. Consequently, Ni-MOLs serve as an efficient electron acceptor with robust interfacial coupling to CdSe, accelerating interfacial electron extraction, suppressing bulk carrier recombination, and thereby preserving more long-lived photogenerated carriers to drive the photocatalytic hydrogen evolution reaction.

To further understand the intrinsic relationship between the band structure of the CNM-*x* composites and the enhanced photocatalytic hydrogen evolution performance, the conduction band positions of CdSe and Ni-MOLs are determined by Mott–Schottky analysis. As shown in Fig. 8a and b, the positive slopes of the Mott–Schottky plots indicate that both CdSe and Ni-MOLs are characteristic n-type semiconductors. From the intercepts, the flat-band potentials of CdSe and Ni-MOLs are determined to be −0.80 and −0.60 V (*vs.* SCE), respectively. In general, the conduction band potential (ECB) of an n-type semiconductor is 0.2 V more negative than its flat-band potential. Accordingly, the ECB values for CdSe and Ni-MOLs are

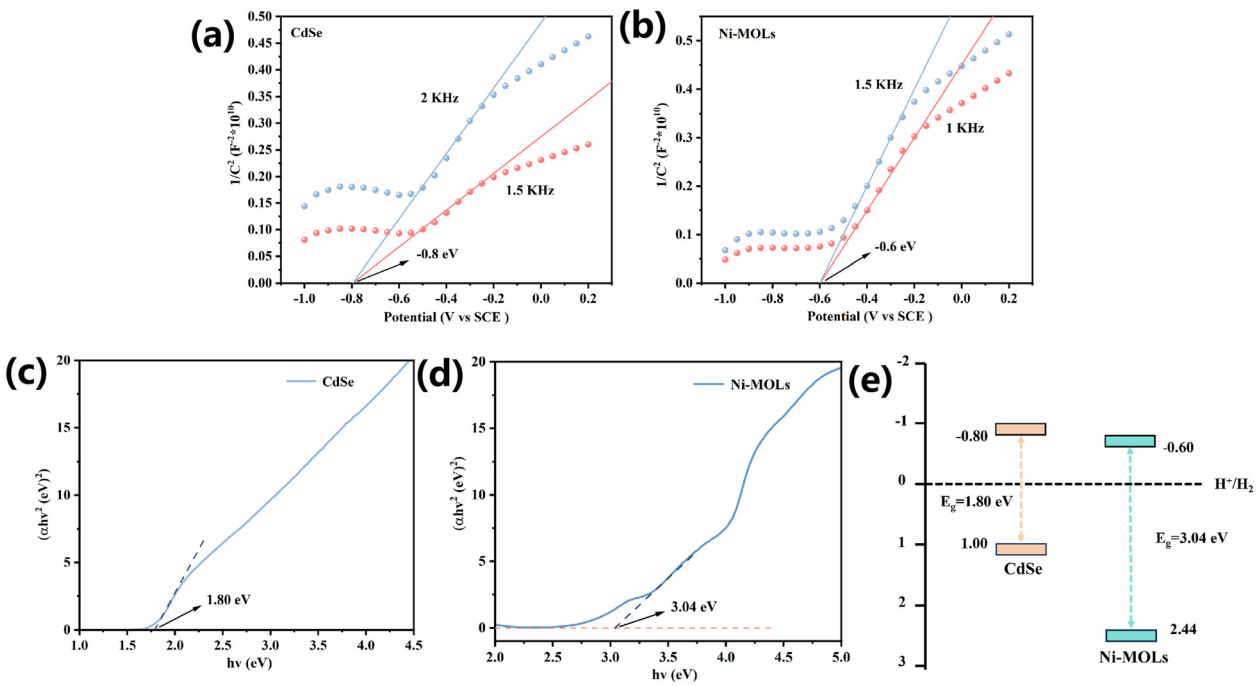

Fig. 8 Mott–Schottky plots of (a) CdSe and (b) Ni-MOLs. Tauc plots of (c) CdSe and (d) Ni-MOLs. (e) Schematic band alignment.

calculated as −1.00 and −0.80 V, which correspond to −0.80 and −0.60 V (*vs.* NHE), respectively.

Furthermore, the band gap energies (E_g) are determined to be 1.80 eV for CdSe and 3.04 eV for Ni-MOLs using Tauc plots derived from the Kubelka–Munk function (Fig. 8c and d). Based on the empirical equation $E_g = E_{VB} - E_{CB}$, the valence band positions (E_{VB}) of the two materials are estimated to be 1.00 and 2.44 V (*vs.* NHE), respectively. The overall band alignments of CdSe and Ni-MOLs are summarized in Fig. 8e, providing a theoretical foundation for deciphering the photocatalytic reaction mechanism.

To gain deeper theoretical insight into the interfacial charge transfer mechanism and the intrinsic nature of the photocatalytic hydrogen evolution reaction, density functional theory (DFT) calculations are performed. Fig. 9a–c displays the optimized structural models of pristine CdSe, Ni-MOLs, and the CNM-0.5 composite. Based on electrostatic potential calculations, the work functions (Φ) of pristine CdSe and Ni-MOLs are determined to be 4.49 eV and 4.78 eV, respectively (Fig. 9d and e). According to the relationship between the Fermi level and the work function ($E_f = E_{vac} - \Phi$), CdSe possesses a higher Fermi level than Ni-MOLs. Consequently, upon interfacial contact, electrons spontaneously migrate from CdSe to Ni-MOLs until the Fermi levels align at equilibrium, which is in good agreement with the *in situ* XPS results.

To visualize the interfacial charge redistribution, the three-dimensional charge density difference and the planar-averaged charge density difference along the direction perpendicular to the interface are calculated for the CNM-0.5 composite (Fig. 9f and g). The charge density difference map clearly reveals that the electron-depletion region is predominantly located on the CdSe side, whereas electron accumulation is concentrated on the Ni-MOLs side. The corresponding planar-averaged charge density difference profile quantitatively confirms a net charge transfer of 4.92 e across the interface, verifying the directional migration of electrons from CdSe to Ni-MOLs and indicating robust interfacial electronic coupling.

Furthermore, hydrogen adsorption models are constructed for pristine CdSe and the CNM-0.5 composite to evaluate the Gibbs free energy of hydrogen adsorption (ΔG) (Fig. 9h–j). The calculated ΔG decreases from 0.62 eV for pristine CdSe to 0.55 eV for CNM-0.5. This notable reduction in the thermodynamic energy barrier signifies that the formation of the heterostructure optimizes the hydrogen evolution thermodynamics, thereby facilitating the photocatalytic process.

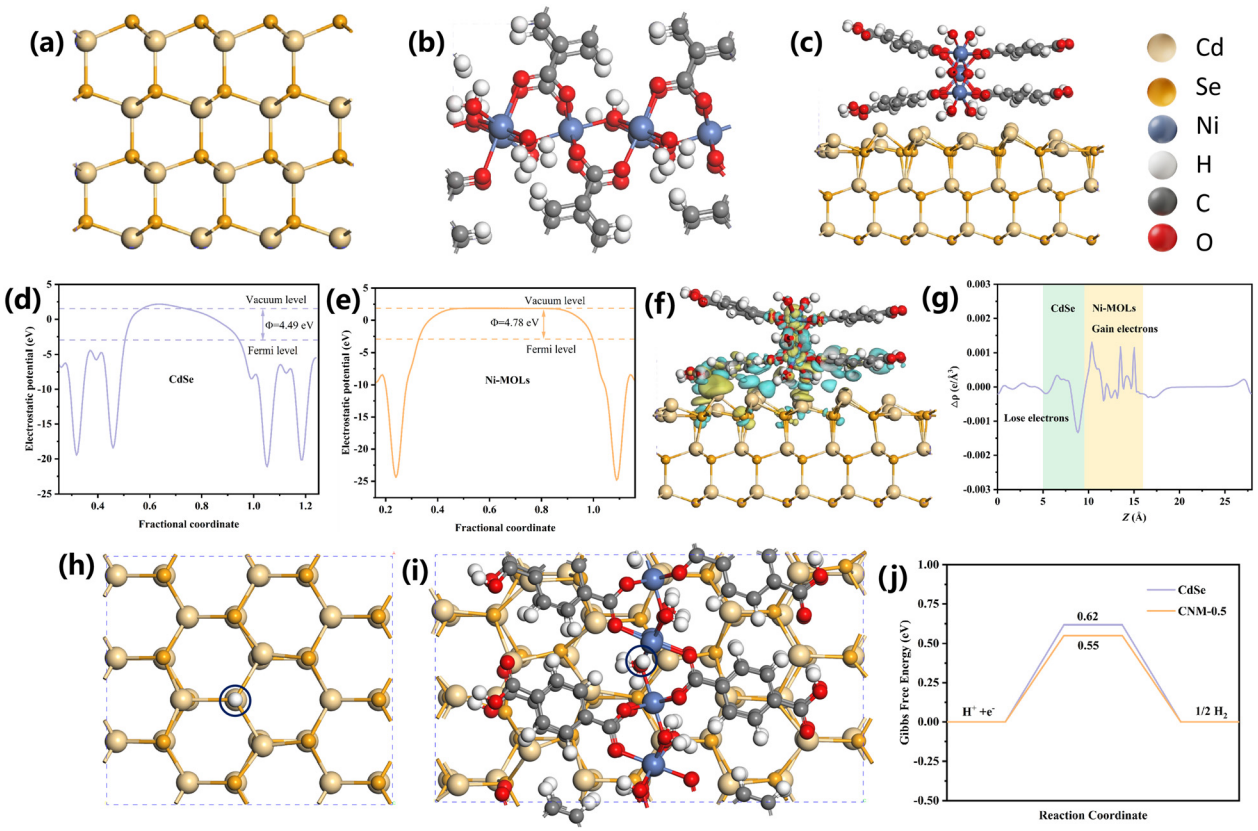

Fig. 9 The optimized structural models of (a) CdSe, (b) Ni-MOLs, and (c) CNM-0.5. Electrostatic potential profiles and calculated work functions of (d) CdSe and (e) Ni-MOLs. (f) 3D charge density difference of CNM-0.5 (the electron depletion and accumulation are depicted in yellow and cyan, respectively). (g) Planar-averaged charge density difference along the *z* direction across the interface. (h and i) Optimized adsorption configurations of H on CdSe and CNM-0.5. (j) Calculated Gibbs free energy diagram of hydrogen adsorption (ΔG).

 This journal is © The Royal Society of Chemistry 2026

Combining experimental characterizations with DFT calculations, the construction of a typical type-II heterojunction between CdSe and Ni-MOLs is unambiguously confirmed, which efficiently drives spatial separation and directional migration of photogenerated carriers. Under visible-light illumination, CdSe is excited to generate electron–hole pairs. Driven by the built-in electric field arising from the staggered band alignment, photogenerated electrons rapidly transfer from the conduction band (CB) of CdSe to that of Ni-MOLs, where protons are reduced to H_2 at the active Ni sites. Concurrently, photogenerated holes in the valence band (VB) of CdSe are rapidly scavenged by the Na_2S/Na_2SO_3 sacrificial agent in reaction system.

Conclusions

In conclusion, a distinctive 1D/2D CNM-*x* heterojunction photocatalyst has been engineered *via* a straightforward *in situ* solvothermal strategy. Under visible-light irradiation, the optimized CNM-0.5 composite achieves a remarkable hydrogen evolution rate of 10.77 mmol g^{-1} h^{-1}, which is 38 and 160 times higher than those of pristine CdSe and Ni-MOLs, respectively. Mechanistic investigations demonstrate that in this architecture, 1D CdSe nanorods with broadband visible-light response serve as the primary light harvesters, while 2D Ni-MOLs act as efficient electron sinks. The well-matched type-II band alignment builds an interfacial built-in electric field that drives directional electron transfer from CdSe to Ni-MOLs, thereby facilitating the rapid spatial separation of photogenerated charge carriers, accelerating interfacial kinetics, and lowering the hydrogen adsorption energy barrier. This study highlights the synergistic effect of the 1D/2D heterostructure in optimizing light harvesting and charge separation, offering a promising strategy for the rational design of advanced CdSe- or MOLs-based photocatalytic systems.

Author contributions

H. Zhao: investigation, validation, writing – original draft. Y. Li: conceptualization, methodology. Y. Liao: writing – review & editing. J. Meng: data curation. Q. Zhou: formal analysis. Y. Wei: validation. Y. Hu: formal analysis. M. Zhang: validation. B. Deng: formal analysis. Y. Huang: validation. Wei-Lin Dai: funding acquisition, project administration, supervision, writing – review & editing, visualization.

Conflicts of interest

The authors declare that they have no known competing financial interests or personal relationships that could have appeared to influence the work reported in this paper.

Data availability

The authors confirm that the data supporting the findings of this study are available within the article and its supplementary information (SI).

Supplementary information: the SI includes material synthesis, instruments employed, and testing procedures, as well as SI figures and tables related to material characterization and performance properties. See DOI: https://doi.org/10.1039/d6cy00639f.

Acknowledgements

This work was funded by the National Key Research and Development Program of China (2021YFA1501404), and the Science and Technology Commission of Shanghai Municipality (2024ZDSYS02).

References

1 Y. Liu, X. Xin, Y. Shi, Z. Zhao, J. Tan, D. Yang and Z. Jiang, *Chem. Eng. J.*, 2024, **482**, 149193.
2 Q. Liu, C. Wang, H. Wang, L. Li, X. Zhang, R. Zhao, J. Han and L. Wang, *Int. J. Hydrogen Energy*, 2024, **81**, 66–74.
3 L. Jiang, D. Wu, Z. Huang, F. Chen, K. Chen, A. B. Ibragimov and J. Gao, *Inorg. Chem.*, 2024, **63**, 14761–14769.
4 Z. Pei, H. Zhang, D. Luan and X. W. Lou, *Matter*, 2023, **6**, 4128–4144.
5 D. Y. Lee, C. Y. Shin, S. J. Yoon, H. Y. Lee, W. Lee, N. K. Shrestha, J. K. Lee and S.-H. Han, *Sci. Rep.*, 2014, **4**, 3930.
6 D. Y. Lee, D. V. Shinde, S. J. Yoon, K. N. Cho, W. Lee, N. K. Shrestha and S.-H. Han, *J. Phys. Chem. C*, 2014, **118**, 16328–16334.
7 X. Chen, *ACS Nano*, 2024, **18**, 1–3.
8 J. Ma, L. Li, Y. Zhang, J. Qian and X. Wang, *Chin. J. Struct. Chem.*, 2024, **43**, 100466.
9 G. Yang, D. Wang, Y. Wang, W. Hu, S. Hu, J. Jiang, J. Huang and H.-L. Jiang, *J. Am. Chem. Soc.*, 2024, **146**, 10798–10805.
10 H. Yang, C. Yang, N. Zhang, K. Mo, Q. Li, K. Lv, J. Fan and L. Wen, *Appl. Catal., B*, 2021, **285**, 119801.
11 S. Guo, L. Zheng, X. Wang, H. Yang, T. Wang, L. Li, Y. Zhang, G. Zhao and T. Li, *J. Colloid Interface Sci.*, 2024, **674**, 902–912.
12 D. Y. Lee, E.-K. Kim, N. K. Shrestha, D. W. Boukhvalov, J. K. Lee and S. H. Han, *ACS Appl. Mater. Interfaces*, 2015, **7**, 18501–18507.
13 H. Yang, F. Chen, X. Wang, J. Qian, J. Wang, J. Li, C. Lv, L. Li, S. Bandaru and J. Gao, *Adv. Funct. Mater.*, 2025, **35**, 2419978.
14 B. Chang, H. Zhang, S. Sun and G. Zhang, *Carbon Energy*, 2024, **6**, e491.
15 F. Raziq, C. Feng, M. Hu, S. Zuo, M. Z. Rahman, Y. Yan, Q.-H. Li, J. Gascon and H. Zhang, *J. Am. Chem. Soc.*, 2024, **146**, 21008–21016.
16 G. Yu, L. Liu, C. Zhao, S. Guo, H. Meng, Y. Zhu and X.-M. Zhang, *Chem. Eng. J.*, 2024, **494**, 153099.
17 J. Bai, J. Wang, H. Zheng, X. Zhao, P. Wu, L. Pei and J. Wang, *Small*, 2023, **19**, 2305024.

18 Y. Zhang, X. Wang, S. Shao, X. Lu, C. Feng, H. Jia, S. Luo and J. Ye, *Appl. Catal., B*, 2024, **349**, 123893.
19 C. Ge, J. Hu, X. Liu, Y. Song, C. Liu and Z. Zou, *Acta Phys.-Chim. Sin.*, 2026, **42**, 100154.
20 C. Liu, W. Xiao, X. Liu, Q. Wang, J. Hu, S. Zhang, J. Xu, Q. Zhang and Z. Zou, *J. Mater. Sci. Technol.*, 2023, **161**, 123–135.
21 F. Leng, H. Liu, M. Ding, Q.-P. Lin and H.-L. Jiang, *ACS Catal.*, 2018, **8**, 4583–4590.
22 W. Fan, H. Chang, J. Zhong, J. Lu, G. Ma, H. Zhang, Z. Jiang and G. Yin, *Sep. Purif. Technol.*, 2024, **330**, 125258.
23 J. Li, H. Chang, S. Feng, H. Jian, Q. Shen, X. Liu, H. Jia and J. Xue, *Chem. Eng. J.*, 2024, **498**, 155542.
24 S. Liu, C. Zhang, Y. Sun, Q. Chen, L. He, K. Zhang, J. Zhang, B. Liu and L.-F. Chen, *Coord. Chem. Rev.*, 2020, **413**, 213266.
25 Y.-M. Lin, W.-W. Cheng, L.-C. Zhang, X.-F. Chen, R. Chen, S. Wang, Q. Yang, J. Wang and J.-D. Xiao, *Small*, 2025, **21**, 2411388.
26 A. Wang, L. Zhang, X. Li, Y. Gao, N. Li, G. Lu and L. Ge, *Chin. J. Catal.*, 2022, **43**, 1295–1305.
27 C. Zheng, Y. Guo, C. Zhang, X. Cao and J. Wan, *Appl. Catal., B*, 2025, **365**, 124879.
28 Y. Yu, W. Yan, X. Wang, P. Li, W. Gao, H. Zou, S. Wu and K. Ding, *Adv. Mater.*, 2018, **30**, 1705060.
29 Z. Qin, F. Xue, Y. Chen, S. Shen and L. Guo, *Appl. Catal., B*, 2017, **217**, 551–559.
30 X.-L. Zhai, J. Liu, L.-Y. Hu, J.-C. Bao and Y.-Q. Lan, *Chem. – Eur. J.*, 2018, **24**, 15930–15936.
31 J. Shen, C. Luo, S. Qiao, Y. Chen, Y. Tang, J. Xu, K. Fu, D. Yuan, H. Tang, H. Zhang and C. Liu, *ACS Catal.*, 2023, **13**, 6280–6288.
32 Z. Liu, Y. Zhang, Y. Wu, B. Yang, Z. Zhou and Z. Jin, *J. Mater. Sci. Technol.*, 2025, **233**, 48–57.
33 R. Xiong, C. Tang, K. Li, J. Wan, W. Jia, Y. Xiao, B. Cheng and S. Lei, *J. Mater. Chem. A*, 2022, **10**, 22819–22833.
34 S. Liu, Y. Yang, W. Xiao, S. Xia, C. Jin, W. Wang, S. Li, M. Zhong, S. Wang and C. Chen, *Int. J. Hydrogen Energy*, 2023, **48**, 32729–32738.
35 R. Yang, W. Mu, L. He, J. Meng, X. Bi, W. Luo, S. Luo and X. Lei, *Chem. Eng. J.*, 2025, **503**, 158495.
36 H. Zhang, C. Shao, Z. Wang, J. Zhang and K. Dai, *J. Mater. Sci. Technol.*, 2024, **195**, 146–154.
37 W. Wu, N. Zhang and Y. Wang, *Adv. Funct. Mater.*, 2024, **34**, 2316604.
38 Z. Liu, E. Cui, X. Wang and Z. Jin, *Chem. Eng. J.*, 2024, **486**, 150060.
39 X. Chen, Z. Li, J. Yuan and X. Hao, *ChemCatChem*, 2025, **17**, e202401624.
40 Z. Fan, X. Guo, M. Yang and Z. Jin, *Chin. J. Catal.*, 2022, **43**, 2708–2719.
41 R. Shi, Y. Cao, Y. Bao, Y. Zhao, G. I. N. Waterhouse, Z. Fang, L.-Z. Wu, C.-H. Tung, Y. Yin and T. Zhang, *Adv. Mater.*, 2017, **29**, 1700803.
42 W. D. Kim, J.-H. Kim, S. Lee, S. Lee, J. Y. Woo, K. Lee, W.-S. Chae, S. Jeong, W. K. Bae, J. A. McGuire, J. H. Moon, M. S. Jeong and D. C. Lee, *Chem. Mater.*, 2016, **28**, 962–968.
43 C. Li, X. Zou, W. Lin, H. Mourad, J. Meng, Y. Liu, M. Abdellah, M. Guo, K. Zheng and E. Nordlander, *ACS Appl. Nano Mater.*, 2021, **4**, 6280–6289.
44 R. Lv, K. Ye, W. Zhang, H. Chen, R. Zhao, H. Wu and M. Chen, *Colloids Surf., A*, 2024, **684**, 133143.
45 T. Le Huec, A. López-Francés, I. Abánades Lázaro, S. Navalón, H. G. Baldoví and M. Giménez-Marqués, *ACS Nano*, 2024, **18**, 20201–20212.
46 P. Dong, K. Gao, L. Zhang, H. Huan, M.-H. Xie, X.-L. Yang and J. Zhang, *Appl. Catal., B*, 2024, **357**, 124297.
47 J. Ma, L. Fan, X. Wang, L. Li, Y. Zhang, G. Zhao, B. Chai and J. Gao, *Surf. Interfaces*, 2024, **54**, 105174.
48 L. Li, X. Wang, H.-X. Liu, S.-S. Xia, Z. Chen and J. Ye, *J. Catal.*, 2024, **429**, 115249.
49 H. Deng, J. Wang, Y. Ouyang, D. Li, Y. Xiao, Q. Zhang and S. Huang, *Appl. Surf. Sci.*, 2023, **622**, 156853.
50 D. Y. Lee, I. Lim, C. Y. Shin, S. A. Patil, W. Lee, N. K. Shrestha, J. K. Lee and S.-H. Han, *J. Mater. Chem. A*, 2015, **3**, 22669–22676.
51 S.-S. Xia, L. Li, C. Bao, J. Wu, C. Li, X. Wang, J. Gao, J. Hu, X. Wang and Z. Chen, *J. Catal.*, 2024, **433**, 115488.
52 M. Zhao, Y. Huang, Y. Peng, Z. Huang, Q. Ma and H. Zhang, *Chem. Soc. Rev.*, 2018, **47**, 6267–6295.
53 Z. Wang, M. Wang, J. Song, J. Wu and Z. Li, *Mater. Chem. Front.*, 2023, **7**, 2651–2660.
54 W. Cheng, X. Zhao, H. Su, F. Tang, W. Che, H. Zhang and Q. Liu, *Nat. Energy*, 2019, **4**, 115–122.
55 H. Yu, X. Wu, Q. Mu, Z. Wei, Y. Gu, X. Yuan, Y. Lu, Z. Deng and Y. Peng, *Chin. Chem. Lett.*, 2021, **32**, 3833–3836.
56 J. Ran, J. Qu, H. Zhang, T. Wen, H. Wang, S. Chen, L. Song, X. Zhang, L. Jing, R. Zheng and S.-Z. Qiao, *Adv. Energy Mater.*, 2019, **9**, 1803402.
57 L. Lv, G. Shen, H. Feng, Y. Liu, H. Liu, H. Zhang, Z. Wang and Y. Wang, *ACS Appl. Mater. Interfaces*, 2024, **16**, 54456–54466.
58 K. Niu, Y. Xu, H. Wang, R. Ye, H. L. Xin, F. Lin, C. Tian, Y. Lum, K. C. Bustillo, M. M. Doeff, M. T. M. Koper, J. Ager, R. Xu and H. Zheng, *Sci. Adv.*, 2017, **3**, e1700921.
59 Z. Wang, L. Cao, H. Hu and C. Wang, *Acc. Chem. Res.*, 2025, **58**, 812–823.
60 Q. Li, H. Chang, G. Gao, H. Jian, W. Liu, H. Jia, J. Xue, H. Liu and Q. Shen, *Sep. Purif. Technol.*, 2025, **353**, 128444.
61 H. Feng, X. Zhang, Q. Yao, Y. Zhou, M. He, Y. Liu, A. Zhang and X. Bu, *J. Alloys Compd.*, 2024, **976**, 173235.
62 X. Wang, X. Wang, H. Yang, A. Meng, Z. Li, L. Yang, L. Wang, S. Li, G. Li and J. Huang, *Chem. Eng. J.*, 2022, **431**, 134000.
63 R. Huang, W. Li, L. Geng, M. Dong, Y. Li, Y. Fan, L. Yang, Y. Liu and H. Han, *Int. J. Hydrogen Energy*, 2024, **89**, 898–906.
64 Z. Fan, Y. Liu, X. Guo and Z. Jin, *Int. J. Hydrogen Energy*, 2023, **48**, 19137–19152.
65 W. Yang, M. Xu, K.-Y. Tao, J.-H. Zhang, D.-C. Zhong and T.-B. Lu, *Small*, 2022, **18**, 2200332.
66 C. Ren, W. Li, H. Li, X. Ma, X. Li, H. Fan, M. Dong, Y. Li and N. Chen, *J. Alloys Compd.*, 2021, **872**, 159691.
67 C. Liu, S. Wang, J. Sun, Z. Yu, Y. Song, Q. Zhang and Z. Zou, *Appl. Surf. Sci.*, 2026, **725**, 165781.

 This journal is © The Royal Society of Chemistry 2026

68 M. Wang, H. Yu, N. Yang and K. Yu, *Sep. Purif. Technol.*, 2025, **354**, 128919.
69 H. Ma, J. He, Z. Li, L. Dong, S. Guo, X. Zhu, D. Li, L. Zang, L. Shi and T. Ba, *Ind. Crops Prod.*, 2022, **189**, 115829.
70 W. Yang, H.-J. Wang, R.-R. Liu, J.-W. Wang, C. Zhang, C. Li, D.-C. Zhong and T.-B. Lu, *Angew. Chem., Int. Ed.*, 2021, **60**, 409–414.
71 C. Liu, H. Yu, W. Xiao, C. Gu, J. Yu, J. Li, J. Song, Y. Song, T. Sun and Z. Zou, *Appl. Surf. Sci.*, 2025, **682**, 161717.

This journal is © The Royal Society of Chemistry 2026